Macalester Journal of Physics and Astronomy

Volume 11
Issue 1 *Spring 2023*

Article 18

June 2023

Development of a Particle-in-Cell/Monte Carlo Simulation for Weakly Ionized Plasmas

Xiaochuan (Chloe) Zheng
Macalester College, xzheng@macalester.edu

James Doyle
doyle@macalester.edu

Development of a Particle-in-Cell/Monte Carlo Simulation for Weakly Ionized Plasmas

Abstract

A plasma is a gaseous system that contains large numbers of electrons and ions that are subject to forces produced by electric and magnetic fields. Weakly ionized plasmas, where the plasma density is much lower than the background gas density, are common in laboratory, atmospheric, and astrophysical situations. Theoretical calculations of plasma properties are challenging due to the complexity of the differential equations used to characterize fundamental physics. Particle-in-cell (PIC) simulations bypass the mathematical difficulties associated with analytic models, at the expense of more complex and time-consuming computer calculations. In this work we developed a one dimensional PIC simulation of a weakly ionized plasma. We use a Monte Carlo technique to include a simplified model of electron-gas and ion-gas collisions. The results of preliminary simulations give good qualitative agreement with simplified theoretical models of plasma sheath formation and ambipolar diffusion.

Keywords

Particle-In-Cell, Monte Carlo Sampling, weakly ionized plasmas, plasma simulation

Development of a Particle-in-Cell/Monte Carlo Simulation for Weakly Ionized Plasmas

Xiaochuan (Chloe) Zheng

Advisor: James R. Doyle

Department of Physics and Astronomy

Macalester College

May 1, 2023

Abstract

A plasma is a gaseous system that contains large numbers of electrons and ions that are subject to forces produced by electric and magnetic fields. Weakly ionized plasmas, where the plasma density is much lower than the background gas density, are common in laboratory, atmospheric, and astrophysical situations. Theoretical calculations of plasma properties are challenging due to the complexity of the differential equations used to characterize fundamental physics. Particle-in-cell (PIC) simulations bypass the mathematical difficulties associated with analytic models, at the expense of more complex and time-consuming computer calculations. In this work we developed a one dimensional PIC simulation of a weakly ionized plasma. We use a Monte Carlo technique to include a simplified model of electron-gas and ion-gas collisions. The results of

preliminary simulations give good qualitative agreement with simplified theoretical models of plasma sheath formation and ambipolar diffusion.

Acknowledgements

I would like to express my gratitude to the following people, without whom this research project would not have been possible.

First and foremost, I would like to thank Professor James Doyle for offering this research opportunity and guiding me through the process. I would like to thank Prof. Doyle for always being so helpful, encouraging, and patient.

I would also like to thank my friends, Cai Dekai and Ou Yetongsen, for their continuous support and faith in me.

I would like to thank my parents for their investment in my education.

Last but not least, I would like to thank the Macalester Physics and Astronomy Department for a community with shared curiosity in physics and nature, and the academic preparation I have gained for my future career.

Contents

Chapter I: Introduction

A. Overview of Plasma Physics

1. Plasma Basics

Plasma is one of the four fundamental states of matter, along with solid, liquid, and gas. It exists in many forms in nature and has a wide range of applications in science and technology. A plasma usually consists of electrons, positively charged ions, and sometimes negative ions, but in the present work we will ignore the possible presence of negative ions. If there is no neutral background gas the plasma is said to be fully ionized. If there is a neutral background gas that could contain neutral atoms or molecules, the plasma is said to be partially ionized. If the concentration of background gas is much greater than the charge particle density, the plasma is called weakly ionized.

Following the definition of the degree of ionization $\chi = \frac{n_e}{n_n + n_e}$, where n_e and n_n denote the electron density and the neutral gas density respectively ,a weakly ionized plasma usually has a χ of lower than 10^{-6}. Weakly ionized plasmas are also usually not in thermal equilibrium, typically having low background gas and ions temperatures and high electron temperature ($T_e \gg T_i \approx T_g$). Many plasmas of interest are weakly ionized,

including Earth's ionosphere, stellar chromospheres, and most engineered plasmas in laboratories [1]. Fully ionized plasmas include stars and plasmas used for terrestrial fusion energy.

In general plasmas are characterized by the plasma density n_p and the electron and ion temperatures T_e and T_i. For weakly ionized plasmas the background gas density n_{gas} is also specified (often as an equivalent pressure at 25 C). For weakly ionized plasmas studied in laboratories and used in plasma processing applications, the ion temperature is around 300~600K, the electron temperature 10000~100000K, the plasma density $10^{13} \sim 10^{18}\ m^{-3}$, and the gas density $10^{19} \sim 10^{24}\ m^{-3}$.

Quasi-neutrality is an important property of a plasma. This means the number of negative and positive charges in the system is nearly the same. Due to the high strength of the electrostatic interaction, separation of positive and negative particles requires high potential energy. Therefore, on large distance scales, the system appears neutral. However, this neutrality is quasi- neutrality because at sufficiently small scales there can be large variations in the local charge density and electric fields. The scale for deviations from neutrality is known as the *Debye length* and will be discussed further below.

2. The Debye Length

When a single charged particle is immersed in the plasma, it will attract local particles with the opposite sign of charge and repel those that possess the same. An observer located far from this single particle will see the combined potential of the particle and its associated "cloud" of surrounding charges. Since the cloud has an opposite polarity, the cloud potential will partially cancel the single particle's potential. The phenomenon of this cancellation is called shielding, or screening [2]. The Debye length is a measure of this shielding distance. It could also be interpreted as the minimum neutrality distance, meaning that over this distance the quasi-neutrality may break down. The expression for the Debye length is

$$\lambda_D = \left(\overline{\epsilon n_0 k_e T_{2e}} \right)_{1/2} \qquad (1.1)$$

where n is the plasma density and T_e is the electron temperature. Debye length is an important property of plasma. It determines the ability of the plasma to shield out electric potentials that are applied to the plasma. In particular, plasmas in contact with a material boundary will deviate from quasi-neutrality in the region of the boundary, depending on the boundary condition. The region of deviation from quasi-neutrality is called the plasma sheath. Note that λ_D increases with increasing electron temperature and decreases with increasing plasma density; this will be important in our discussion of results below.

3. Plasma sheaths

The formation of plasma sheaths can be described as follows. When a system is confined in a vessel, which is often the case for laboratory experiments [3], the electrons encounter boundaries and leave the system more quickly than ions due to their typically higher temperature and much lower mass. The quick loss of the electrons results in a positive net charge in the remaining plasma near the boundary. The result is that the potential is higher in the quasi-neutral region of the plasma than at the wall.. This positively increased potential tends to trap electrons, and slow down the overall electron flux to the wall. On the other hand, with the wall potential at more negative potential than the plasma the ion flux will increase. The region between the wall and the steady potential in the system is called the plasma sheath. The sheath acts effectively as a way of reducing the electron flux while increasing the ion flux,, and thus moves towards balancing the initial large difference in the loss rate of the electrons and ions. In the special case of a floating surface (i.e. a surface that cannot conduct away the charges) the electron and positive ion flux to the surface must cancel in the steady-state. In this case the surface has a net negative charge due to the initial higher flux of electrons. In general, however, the relative electron and ion fluxes to the confining walls will depend on boundary conditions imposed on the walls.

The formation of the sheath described above is due to an effect called ambipolar diffusion. In general, if we start with a quasi-neutral plasma that is initially bounded, the higher mobility and diffusivity of the electrons will always result in an charge imbalance in the plasma over time. However, this charge imbalance results in an electric field that

counters the electron diffusion and enhances the ion transport. In the steady-state an electric field is generated which tends to equalize the flow of both ions and electrons. The simple theory of ambipolar diffusion is an idealized phenomena that ignores imposed boundary conditions on the plasma, as well as any potential evolution in the plasma properties such as the electron temperature. Nevertheless, it is a useful conceptual tool to understand passive charge transport in plasmas, as opposed to plasma that are driven by an external energy source.

4. Glow Discharges

In the laboratory, plasmas can be created by applying a sufficiently large voltage across two electrodes that contains a gas. Under the right gas density conditions, the gas will "break down" and become conductive and a current will flow [4]. The breakdown occurs when an electron spontaneously appears in the electrode gas (for example from a cosmic ray). The electron gains energy from the applied electric field, and will eventually have enough energy to collisionally ionize the gas. Electron multiplication thus occurs with the generation of ions. Ions striking the lower voltage electrode (the cathode) will result in emission of electrons from the electrode (a process known as secondary electron emission), and the plasma current is a self-sustaining discharge. Energy is dissipated in the discharge through collisions and excitation and ionization of the gas and impact of the ions and electrons on the electrodes and walls. This energy is supplied to the discharge by the external power supply that is providing the voltage across the electrodes. Because of the electron collisional excitation process, the discharge emits photons and is therefore commonly referred to as a glow discharge. This type of discharge is the source of light from fluorescent lights and "neon" signs.

5. Afterglows

Glow discharges have a complicated structure including different kinds of sheaths at the electrodes and at the other confining surfaces [5]. However, in the central regions of the discharge a quasi-neutral plasma, called the positive column, is formed. In this region the electrons and ions can be approximately characterized by Maxwell-Boltzmann distributions having T_e and T_i respectively, where $T_e >> T_i$ (see above). A simplified plasma structure can be obtained for short times by abruptly turning off the external power, resulting in a plasma *afterglow*. In this situation the sheaths at the electrodes rapidly collapse and an approximately quasi-neutral plasma fills the inter-electrode region. However, ambipolar diffusion then begins and sheats form at all surfaces, followed by a decay of the plasma as ions and electrons are absorbed at the boundaries. One of our goals with the development of the simulation here is to observe this ambipolar diffusion as well as the evolution of the afterglow over time.

6. The Plasma Frequency

To complete this overview of plasma physics we should mention the plasma frequency ω_p. Just as the Debye length represents a characteristic length scale for the plasma, the plasma frequency represents a characteristic frequency or time scale for a plasma. The plasma frequency is derived by imagining a slight displacement of the electron density with regard to the ion density at t = 0. The restoring electric field force then results in a harmonic oscillation of the electron density. The plasma frequency is given by

$$w_p = \sqrt{\frac{}{qm_e{}^2{}_e n \epsilon_{0p}}}$$

In this work our focus is on the spatial structure of the plasma, but the plasma frequency is important since it determines the appropriate time scale for the time evolution of the afterglow. In particular, our time increment in our simulations should be much less than wp, in order to properly resolve time evolution.

B. Types of plasma calculations

Although plasmas are extensively studied through experiments in the laboratory, these studies need to be supported by theoretical and computational models of plasma structure and evolution. In addition, some plasma conditions that exist in the universe (such as interstellar space) are difficult to replicate in the laboratory, so modeling is needed to fully understand their nature. Therefore, plasma modeling is a valuable and complementary approach in studying the plasma characteristics, development, and interactions.

Plasma modeling provides a means to study in detail the physical and chemical processes that occur in the plasma [6]. Theoretical modeling uses equations of electron and ion transport coupled to external and internally generated electric and magnetic fields to produce analytic expression to analyze the behavior of plasma. However, due to the complexity of the system, especially when collisions are included, these methods require many and often severe approximations. Therefore in most cases this approach is very

approximate and is expected to be only in qualitative and semi-quantitative agreement with experiment results.

Computer simulation of plasma processes can relax many of the approximations made in analytic models. There are several approaches to computational plasma physics. Plasma models with fluid approaches assume local thermodynamic equilibrium and treat particle transport as flow fields. Fluid models are based on particle differential equations that describe the motion of fluids coupled with Maxwell's equations for the electric and magnetic fields. These fluid models describe macroscopic plasma phenomena and reveal how the average plasma parameters evolve in time and space. Fluid approaches are most suitable for dense, fully-ionized plasmas where local thermodynamic equilibrium is a good assumption. However, the coupled fluid-field equations are usually complex and non-linear and the simulations often simplify the equations by neglecting some terms, such as the viscosity effect in the transfer equation or kinetic energy contribution compared to the thermal one, at the expense of accuracy [7]. At the lower pressure characteristic of weakly-ionized laboratory plasmas, the assumption of local thermodynamic equilibrium is usually not valid [8]. Although hybrid models that treat ions and neutral gas as fluids while treating electrons using kinetic or Monte Carlo methods overcome this limitation to some extent, since the problem of local thermodynamic equilibrium is due primarily to the electron dynamics.

The Particle-In-Cell (PIC) simulation method makes the fewest assumptions of commonly used plasma simulation methods. In PIC simulations the motion of charged

particles is treated directly using Newtonian particle mechanics. The particle positions provide the local charge density from which the potentials and fields, and the forces that determine the particle motion can be self-consistently calculated. PIC thus represents a kind of "mean field" approach to the plasma particle dynamics. Of course it is not computationally possible to simulate the motion of individual electrons and ions in a plasma having a density ~ 10^{15} m^{-3}, so the PIC method simulates far fewer (but still statistically significant) numbers of "superparticles". The PIC method has the advantage of making minimal dynamical assumptions. Furthermore, with the addition of Monte Carlo methods to simulate collision phenomena, PIC simulations can incorporate highly accurate collision physics that is not possible in analytic or fluid approaches. However, PIC simulations have important limitations as well, such as being very computationally intensive. In addition, PIC simulations are probably best considered as "numerical experiments" with results that require other types of models to understand the basic physics of the results. Finally we should mention that PIC simulations are sometimes used in conjunction with fluid models to balance the tradeoffs and better simulate the specific plasma scenarios of interest.

C. Overview of this work

In our simulation, we develop a PIC simulation method to study one-dimensional weakly ionized plasmas, using helium as the background gas. The one-dimensional nature of the simulation (approximately experimentally realizable using large electrodes closely spaced) limits the application to electric fields only; including magnetic fields would

require at least two dimensions. We use Monte Carlo sampling methods to include simplified electron-gas and ion-gas collisions. Since the gas density exceeds the plasma density by many orders of magnitude, charged particle-charged particle collisions can be neglected and the electrostatic field that the ions and electrons experience are instead determined by a mean field approach. Monte Carlo sampling is also used to properly initialize the electron and ion velocity distributions. The motivation of this work is mainly to study some basic and important plasma properties, with an emphasis on sheath formation and ambipolar diffusion effects under idealized conditions. In the future the simulation will be further developed to include more realistic collision models and geometries that can be compared with more actual laboratory experiments and more sophisticated theoretical models.

Chapter II. Methods

Discretization

For a practical laboratory plasma system, the charge distribution is essentially continuous. However, in order to numerically calculate the potential and field, we need to discretize space and consequently the charge density, potential, and the electric field.

A. Discretization of charge density ρ

The spacing between grid points is denoted h. For a particle with position x and total charge of q, we first break down the position into an integer that represent the rounded-down grid point i and the fraction f of h to the next grid point:

$$x = i + f \qquad (2.1)$$

We assume this superparticle's charge q will only contribute to the ith and $(i + 1)$th grid points. We assign its charge to the two grids points as follows:

ρ

$_i$ += $q(1-f)$ (2.2) ρ$_{i+1}$

+= qf

(2.3)

B. Discretization of potential ϕ

Poisson's equation for electric potential is :

The first order derivative for a function$\frac{d}{d}$f(x)^2xϕ$_2$ is:= $-\epsilon_0\rho$

Similarly for the second derivative,$f'(x) = \lim_{h\to 0} f(x+hh)-f(x)$

$$f'(x) = \lim_{h\to 0} \underline{f'(x+hh)-f'(x)}$$

$$f'(x) = \lim_{h\to 0} \left(\underline{f(x+2h)h-f(x+h)} - \underline{f(x+hh)-f(x)} \right)/h$$

This gives the discrete form of the second order derivative as a finite difference:

Therefore we can discretize$f$the'(x)electric= $_h$lim→potential$_0$
$\underline{f(x+2h)-2}$using$_h$$f_2$$\underline{(x+h)}$this$\underline{+f(x)}$method, denoting the grid

point as the index i: ϕ

In our simulation, the index number $\underline{d}d_2x\underline{\phi}_2 = i$ goes $\phi_{i+1} - (\text{from} \Delta 2\phi x)_{i+2}\,\phi 0_{i-1}$ to $= -\epsilon\rho_{0i}$, where the points 0 and

are the boundary points. The interior points Ng go from $+\ 11$ to . The charge

density is Ng only $+\ 1$ defined on the interior points while the potential includes Ng the

boundaries. The

boundary potentials are specified at the start of the simulation ϕ as the boundary conditions on ϕ. Using the charge density array determined from the particle positions and the potential boundary potential values, we can calculate the potentials on the interior grid point with indices from 1 to Ng. We can write out the following relations:

$$i = 1: \qquad \phi_0 \overline{-(2\Delta\phi x)_{12} + \phi_2} \qquad = -\epsilon \underline{1}_0 \rho 1$$

$$i = 2: \qquad \phi_1 \overline{-(2\Delta\phi x)_{22} + \phi_3} \qquad = -\epsilon 1_0 \overline{\rho} 2$$

$$\ldots$$

$$i = Ng: \qquad \phi_{Ng-1} \overline{-(2\Delta\phi x_{Ng})_2 + \phi_{Ng+1}} \qquad = -\epsilon 1_0 \overline{\rho} Ng$$

Multiply the *i*th term by its corresponding i:

$$i = 1\text{: } (\phi_0 - 2\phi_1 + \phi_2) \cdot 1 \quad = (-\epsilon^1{}_0 \rho_1) \cdot 1 \cdot (\Delta x)^2 \; i = 2\text{: } (\phi_1 - 2\phi_2 +$$

$$\phi_3) \cdot 2 \qquad = (-\epsilon^1{}_0 \rho_2) \cdot 2 \cdot (\Delta x)^2$$

$$\ldots \; i = Ng\text{: } (\phi_{Ng-1} - 2\phi_{Ng} + \phi_{Ng+1}) \cdot Ng \qquad = (-\epsilon^1{}_0 \rho_{Ng}) \cdot Ng \cdot (\Delta x)^2$$

Now and the we add up all terms. the terms. On the left, all terms cancel out except for the 0th, the Ng,

$$Ng + 1 \; \phi_0 + ((Ng + 1 - 1) - 2(Ng + 1))\phi_{Ng} + \phi_{Ng+1} = -\sum_{i=1}^{Ng} i \, \epsilon^1{}_0 \rho_i$$

$$\cdot (\Delta x)^2$$

Then we solve for ϕ_{Ng}:

$$\phi_0 - (Ng + 1)\phi_{Ng} + \phi_{Ng+1} = -\sum_{i=1} i \frac{1}{\epsilon_0} \rho_i \cdot (\Delta x)^2 \qquad (2.4)$$

$$\phi_{Ng} = \frac{\sum_{i=1}^{Ng} i \frac{1}{\epsilon_0} \rho_i - \phi_0 - \phi_{Ng+1}}{(Ng+1)*(\Delta x)^2} \qquad (2.5)$$

Once we have ϕ_{Ng}, we can solve for the rest of the potential with indices from 1 to

$Ng - 1$ using the relationship

$$i \in \{1, . , Ng - 1\} : \phi_i - 2\phi_{i+1} + \phi_{i+2} = -\epsilon^1{}_0 \rho_{i+1} * (\overline{\Delta x})^2$$

$$i \in \{1, . , Ng - 1\} : \phi_i = -\epsilon^1{}_0 \overline{\rho_{i+1}} * (\Delta x)^2 + 2\phi_{i+1} - \phi_{i+2} \quad (2.7)$$

C. Discretization of electric field E

With the potentials determined at the grid points by the procedure above, we can now calculate the electric field at all of the grid points. The electric field E is related to

$$= \quad - \nabla\phi$$

the electric potential ϕ by E dependent

Since our potential is one-dimensional and on x,

Use finite difference method for the first$E =$order $-$ derivative,$\frac{d}{dx}\phi\, x$ we have:

$$E = -\frac{\phi_{i+1} - \phi_{2i-1}}{2(\Delta x)} \quad (2.8)$$

i

D.Discretization of Equations of Motion

The particle equations of motion need to be discretized in time. For each particle p at timestep n, we have for the acceleration

$$a_{(pn)} = \frac{qEm_{(pn)}}{} \quad (2.9)$$

Where E_p^n is the electric field at the particle p position at the nth time step. E_p^n is determined by using the E values at the two adjacent grid points to the particle, with weights determined by the relative distance to those grid points. From the acceleration we have the updated velocity using the discretized time interval DT

$$v_{(pn+1/2)} = v_{(pn-1/2)} + a_{(pn)} * DT \qquad (2.10)$$

giving the update position as

$$x_{np+1} = x_{np} + v_{pn+1/2} * DT \qquad (2.11)$$

The choice of DT will be described below. The notation v and v refers to the "leap frog" method of calculating the velocity. This is because using the sampled velocities at timestep n assumes that the particle moves at this constant velocity throughout the entire timestep, which is inaccurate since the particle usually has non-zero accelerations. Calculating the particle's displacement during one timestep with a velocity in the middle, that is $v^{n+1/2}$ is thus a better approximation. To implement this idea, immediately after assigning initial velocities to the particles (see below) we adjust the velocity at time = 0 for each particle as

The velocity $v_{-1/2}$ is called the back$v_{-1/2}$velocity$= v_0 -$of0.the5 *particle. $a * DT$

E. Collision Model

In a weakly ionized gas, the electrons and ions collide mostly with the background gas atoms instead of with each other. In this preliminary study we assume that the electron-atom collisions are hard sphere collisions, and the ion-atom collisions are charge-

exchange collisions. The atoms are assumed to be static before scattering. This is a very good approximation for the electron-atom collisions due to the high velocity of the electrons. The case of the charge exchange collisions will be discussed below.

The advantage of hard sphere collisions is that the collision cross section, and the scattering angle versus the impact parameter, have analytic forms. The cross-section for the electron-atom collisions is given by $\sigma = \pi R^2$. This can be thought of as the effective cross sectional area of interaction, where R is the effective radius of interaction. For hard spheres, R is the sum of the radii of the colliding objects. Since the electrons and ions have very small radii compared to those of the atoms, we may consider R as just the radius of a background gas atom. In our simulations R is equal to $5 \cdot 10^{-10} m$. Though larger than the actual radius of the helium atom, a larger R accounts for the additional ion-induced dipole effect that increases the cross section in charged particle - atom collisions.

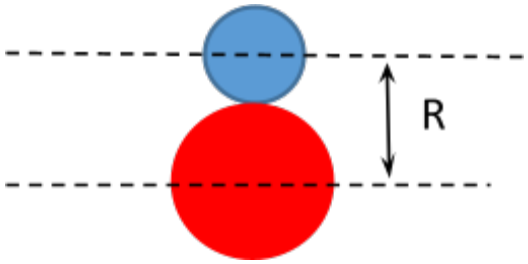

Figure 2.1: An illustration of the effective radius of interaction *R*. For two particles colliding, *R* is the sum of the radii of the two particles.

We define the distance between the centers of the colliding particles to be the impact parameter b, as illustrated in Figure 2.1. The scattering angle θ is illustrated in Figure 2.2.

Figure 2.2: Definition of the impact parameter b.

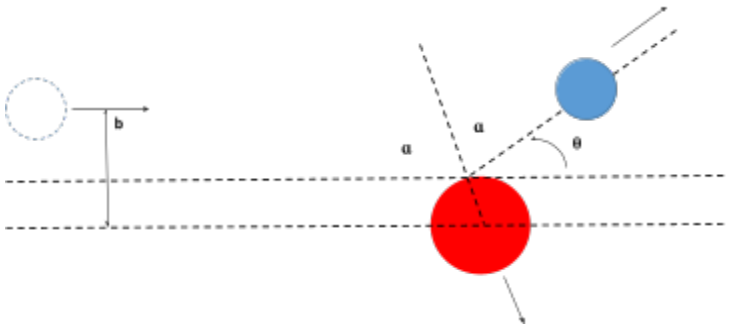

Figure 2.3: The scattering angle θ

In a hard sphere collision, the angle of incidence of the scattering will be equal to the angle of reflection. Define this angle to be α, as denoted in Figure 2.3. The scattering angle is θ, which is the auxiliary angle of α. From the geometry of the scattering model we can find the relationship between θ and α to be:

The impact parameter b is also related to α and θ by: $\theta = \pi - 2\alpha$

$$b = R \cdot sin(\alpha)$$

Therefore, we derive function of the deflection angle θ dependent on b:

$$b = R \cdot sin(\tfrac{\pi}{2} - \tfrac{\theta}{2}) \quad \theta(b) = 2 \cdot cos^{-1}(\tfrac{b}{R}) \qquad (2.9)$$

In our simulation, each scattering event only affects the electron's velocity and we neglect the energy gain of the target gas atoms. However, we do account for the energy loss of the electrons in the collision. The post-collision velocities for both the incident and target particles are given by conservation of energy and momentum for a given scattering angle θ. The change in the electron speed is given by [9]:

$$v_f/v_i = \sqrt{1 - 2m_e m_{gas}/(m_e + m_{gas})^2 \cdot (1 - cos(\theta))} \qquad (2.10)$$

Using this expression, an updated 1-D velocity of an electron after a collision is produced and , in our simulation, the horizontal component of its new velocity vector is generated. However, since $m_e/m_{gas} << 1$, the fractional change ß in the electron speed is very small. This is the primary reason why in weakly ionized plasmas electrons do not readily equilibrate with the background gas and maintain their high temperature.

For an ion, since its mass is comparable to the mass of the helium atom we assume the atom and the ion simply exchange velocity after the collision. That is, after the collision, the incident ion is neutralized and no longer tracked, and the new ion begins with a velocity sampled from the neutral gas Maxwell-Boltzmann distribution. According to Equation 2.10 above, when the masses are comparable there is a very efficient transfer of energy (and momentum) between the collision partners. This is the primary reason why ions tend to be in thermal equilibrium with the background gas in weakly ionized plasmas.

The scattering cross-section determines the mean free path for collisions

$$\lambda = 1/(n_{gas}\,\sigma)$$

where is the number density of the background gas. The probability distribution of free paths is given by

n_{gas}

The mean scattering time is the average$P(x)$ time$=$ 1between$/\lambda \cdot e_{-x/}$scatteringλ events.

For a beam of particles with speed v and given free path Δx, the time Δt is given by

$$\Delta t = \frac{\Delta x}{v}$$

Δx Δt

For a given distance , will be shorter for a higher speed. This means that for a fixed mean free path, the scattering events happen more frequently when the particles are moving faster. As discussed in the section Monte Carlo simulations below, in the simulation the collision time is sampled from the distributions of free paths divided by the relative speed of the collision partners.

F. Monte Carlo Sampling

Monte Carlo sampling refers to the process of using a pseudo-random number generator to sample from a known probability distribution. There are two general methods for doing this of interest to us: direct sampling and rejection sampling.

1. Collision Time

Consider a normalized probability distribution given by P(x). We wish to sample values of x from this distribution using a random process that reproduces the distribution P(x). In the direct sampling method this can be done using

$$RND = \int_0^x P(x')\,dx'$$

Where RND is a pseudo-random number between 0 and 1. According to probability theory [10] when this procedure is repeated many times the resulting distribution of x values will satisfy P(x). For the distributions of free paths given by kinetic theory as P(x) $= \frac{1}{\lambda} e^{-x/\lambda}$, we have:

$$RND = \int_0^{\Delta x} \frac{1}{\lambda} e^{-x'/\lambda}\,dx' = 1 - e^{-\Delta x/\lambda}$$

where λ is the mean free path. Δx is the sampled path. Solve for Δx, we have:

$$\Delta x = -\lambda ln\,(1 - RND) = -\lambda ln\,(RND)$$

The term $(1 - RND)$ can also be written simply as (RND) since the random number ranges from 0 to 1 uniformly. In our simulation it is more convenient to sample collision times rather than free paths. From the collision model we have the expression for the sampled collision time:

$$\Delta t = \frac{\Delta x}{v}$$

where v is the relative speed of the colliding partners and Δx is the sampled path.

Therefore, we can calculate for the sampled collision time:

$$\Delta t = -\overline{\nu^{\lambda}}\, ln\,(RND) = -\,\tau ln\,(RND) \qquad (2.11)$$

The expression $\overline{\nu^{\lambda}}$ is equivalent to the average collision time τ.

2. Impact parameter b

We can also use the direct sampling method to determine the impact parameter b in the collision model. Recall the effective cross sectional area to be πR^2, which means the incident particle can potentially collide with the target particle anywhere within this area with equal probability.

Each value of b is represented by an annulus of area $2\pi b \cdot db$, as illustrated in Figure X.

Therefore, the probability of getting a certain b is proportional to the area of the annulus

$$P(b)db \propto 2\pi bdb = C2\pi bdb$$

where C is a normalization constant:

$$1 = C\int_0^R 2\pi bdb = C2\pi\tfrac{1}{2}R^2$$

Solving for C:

$$C = \frac{1}{\pi R^2}$$

Giving the normalized probability distribution

$$P(b)db = \frac{2}{R^2} b\, db$$

The direct sampling method gives

$$RND = \frac{2}{R^2}\int_0^b b\, db = \frac{b^2}{R^2}$$

Solve for b, we have

$$b = R\sqrt{RND} \qquad (2.12)$$

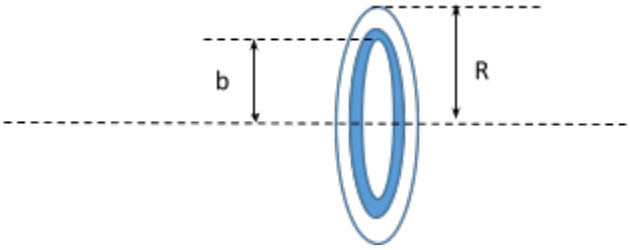

Figure 2.4. Sampling of the collision impact parameter

3. Initial velocities

If the probability distribution P(x) does not have an analytic integral, or the integrated form cannot be easily inverted to give x, the rejection method of sampling can be used. The rejection method has the advantage that any P(x) can be sampled, but the disadvantage of being much more computationally intensive than the direct method. In our simulation we use the rejection sampling method to generate the initial velocities of the particles from the Maxwell-Boltzmann distribution:

$$P(v) = 4\pi(\overline{m_e})^{3/2} e^{-\frac{m 2kT_e v_2}{2\pi kT}} (2.13)$$

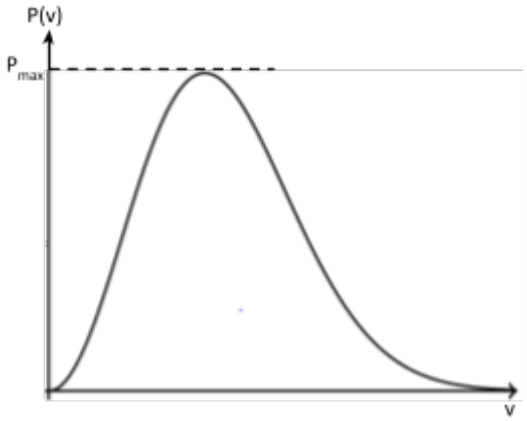

Figure 2.5 The Maxwell-Boltzmann Distribution:

We first re-normalize the distribution so that the maximum value of the curve is equal to 1, and therefore the y axis is P/P_{max} which varies from 0 to 1. The x-axis ranges from 0 to a maximum velocity of our choice that makes all relevant values of velocities included.

In our simulations We chose $v_{max} = 5v_{mp}$ where v_{mp} is the most probable speed.

$$v_{mp} = \sqrt{\frac{3}{m}\frac{kT}{}} (2.14)$$

To perform the rejection sampling method, we first generate a random number RND1 and calculate a test velocity

$$v_{test} = RND1 \cdot v_{max}$$

Draw a box with width of v_{max} and height 1, as demonstrated in Figure X.

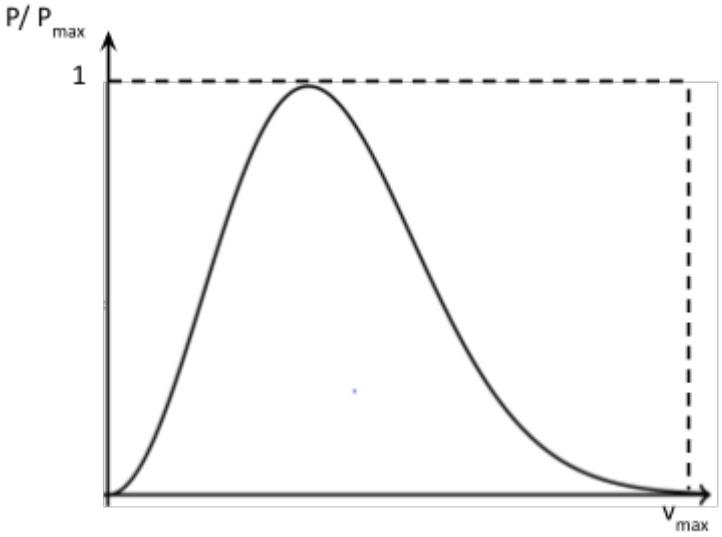

Figure 2.6: The rejection method

Now generate a second random number RND2 as a test probability. Calculate

$P(v_{test})/P_{max}$. If $RND2 < P(v_{test})/P_{max}$, accept v_{test} for a sampling velocity.

Otherwise, generate a new test velocity and a new RND2, until the condition

arrays,$RND2$ we< may $P(v_{test}$sample$)/P_{max}$a velocitysatisfies.forByeachloopingparticlethisthatmethodfollowsoverthetheMaxwell-Boltzmannelectron and ion

distribution.

Assuming the generated velocities represent an isotropic distribution in three-dimensions, we need to sample appropriate values of q and f. Both of these angles can be selected by the direct sampling method. Values for angle ϕ are evenly distributed between 0 and 2π. Therefore,

$$\phi = RND(2\pi) \qquad (2.15)$$

The probability of selecting angle θ will be an proportional to the area of the annular region shown in That is, Figure X below. P

$$(\theta)d\theta = C\,2\pi R\,sin\theta\,Rd\theta$$

Normalize this distribution by $\int\int$. This gives setting $\int_0^{\pi} P(\theta)d\theta = \int_0^{\pi} C\,2\pi R\,sin\theta\,Rd\theta = 1$

The integral of this distribution$P(\theta)d\theta =$can $4\pi 1$beR_2 analytically $2\pi R\,sin\theta\,Rd$solved$\theta =$ easily,$2\underline{1}\,sin\theta$therefore $d\theta$ we use the

direct sampling for selecting the angle θ. Construct and solve the integral:

$$RND = \frac{1}{2}\int_0^{\theta} sin\theta'\,d\theta'$$

Solve for the angle θ: $RND = 12\,(1 - cos\theta)$ $\theta = cos{-1}(1 -$

$2 \cdot RND)$ (2.16)

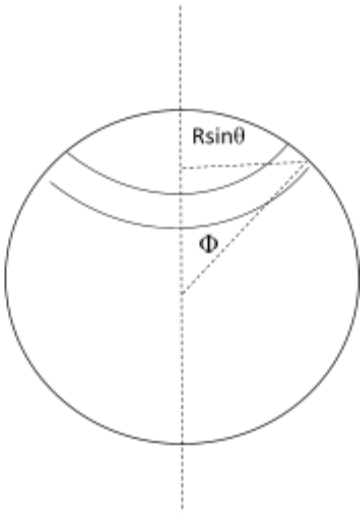

Figure 2.7. Geometry for θ selection

The components of velocity are then

$$v_x = v\ sin\theta\ cos\dot{\phi}$$

$$v_y = v\ sin\theta\ sin\dot{\phi}$$

$$v_z = v\ cos\dot{\theta}$$

In our 1-D program only v_x is affected by the electric fields. However, in order to provide proper tracking during the simulations, and post-collision parameters, v_y and v_z must also be tracked for each particle pre-

G. Summary of the Algorithm

The flow chart below summarizes the algorithm of our simulation. The function that implements the equations of motion 2.9- 2.11 is called the *mover*.

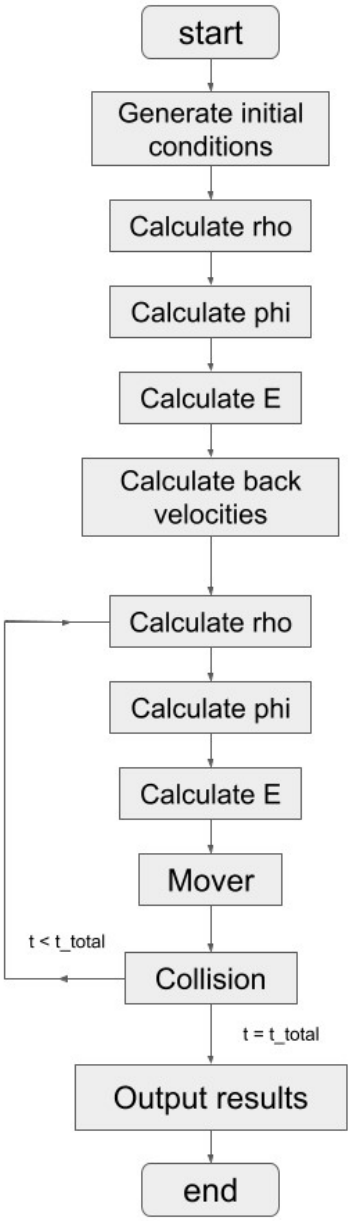

Figure 2.8: Flow chart of the simulation.

H. Limits on DT and H

The plasma frequency is the natural frequency for the system, so for adequate time resolution we want the time increment to be much less than one electron plasma oscillation period:

$$DT \ll \frac{2\pi}{\omega_p} = 2\pi\sqrt{\frac{m_e\epsilon_0}{n_e e^2}}H$$ In addition, to properly resolve the spatial variations, we want the spatial increment to be much less than the Debye length, the characteristic distance scale for the plasma

$$H \ll \lambda = \sqrt{\frac{\epsilon_0 k T_e}{n e^2}}$$

These relationships need to be verified for each set of n_p and T_e conditions.

I. Programming Details

The PIC simulations were implemented in the C++ computer language using a Linux operating system platform. All simulations used initial 20 million (2×10^7) superparticles for each of the electrons and ions. The memory requirements for such large arrays were not supported by the default memory allocations, so stack size and maximum locked memory had to be manually set to *unlimited* for each session. Depending on the total number of time steps simulated (see Chapter V) the run-times ranged from a few minutes to about 12 hours. Python and R-Studio were used in the analysis of the data.

Chapter III. Scaling for Dimensionless Equations

In numerical calculations it is usually desirable to use quantities that are dimensionless to remove the arbitrariness of units. In this chapter we develop the relevant scale factors to turn the discretized equations developed previously into dimensionless quantities.

We have Ng interior points, where boundary points are 0 and $Ng + 1$, therefore we have

$Ng + 1$ intervals with a total length of L, measured in meters. For each dimensionless

interval in the model, the spacing in real unit is:

$$H = \overline{Ng^{L}+1}$$

The time increment DT is given by $DT = f_t * {}^{2}\omega\pi_p$

where ω_p is the plasma frequency. For all of the simulations presented here f_t=0.005. The

simulation takes a total number of times steps Nt. Each time step corresponding to DT is

assigned the dimensionless value of 1.

Each superparticle represents individual particles. Therefore, for each superparticle, N_s

$$Q_e = -N_s e$$

$$M_e = N_s m_e$$

$$Q_i = + N_s e$$

$$M_i = N_s m_i$$

The equations of motion of the p th particle are

$$v_{n+\frac{1}{2}} = \frac{x^{n_p+1} - x^{n_p}}{DT}$$

$$a_{np} = F(\overline{Mx_{pnp}}) = \overline{vDT_{np-\frac{1}{2}}}$$

And the field equations are $F(x_{np}) = Q_p E(x_{np})$

$$E_{ng} = \overline{\phi^{n_g-1}2-H\,\Phi^{n_g+1}}$$

To make these equations dimensionless, $\phi^{n_g-1} - 2H\phi$ we$_{2^{n_g}}$ + introduce $\phi^{n_g+1} = -\epsilon$ the$_{\rho_0{}^{n_g}}$ following quantity that has e

units of J/C = Volts:

$$2M\overline{DT_e H_2 Q_{2\,e}} = \overline{2mD_e T H_{22} e}$$

Therefore, the dimensionless potential would be:

$$(\phi_{ng})' = \frac{}{2MD\phi T_e H n g^2 Q_{2e}}$$

$$(\phi_{ng})' = \phi_{ng}\, 2\underline{D}m\underline{T}_{e2}H\underline{e}_2$$

Recall that $\phi_{ng-1} - 2H\phi_{2ng} + \phi_{ng+1} = -\epsilon\rho_{0gn}$, which means

$$(\phi_{ng-1})' - 2(H\phi_{2ng})' + (\phi_{gn+1})' 2\underline{D}m\underline{T}_{e2}H\underline{e}_2 = -\epsilon\rho_{0ng}$$

Giving the dimensionless charge density

$$(\rho_{ng})' = \rho_{ng}\, 2\underline{D}m\underline{T}_{e2}\epsilon\underline{e}_0$$

Also recall that $E^n g = \phi_{n_{g-1}} 2 \; H \; \phi_{n_{g+1}}$ from. Therefore,

$$(2H)E^n g = (\phi^n g{-}1) - (\phi^n g{+}1)$$

$$(\phi^n g{-}1)' - (\phi^n g{+}1)' = {}_2\underline{D}_m\underline{T}_{e^2}H\underline{e}_2\,(2H)E^n g = (E^n g)'$$

Giving for the dimensionless electric field

The dimensionless position is $(E_{ng})' = E_{ng}\, DmT_{e2}He$

And the dimensionless velocity is: $(x_{np})' = xH_{np}$

The acceleration is: $(v_{np})' = v_{np\ DTH}$

$$a_{np} = = \overline{Q_p EM(_p x^n{}_p)}\ DT\ a_{np}$$

$$= v_{np+\ 12} - v_{np-\ 12}\ (a_{np})' =$$

$$(v_{np+\ 12})' - (v_{np-\ 12})'$$

$$(a_{np})' = (v_{np+\ 12} - v_{np-\ 12})\ \underline{DT}H$$

$$(a_{np})' = \overline{Q_p EM(_p x_{np})}\ DT\ \underline{DT}H$$

Recall that $Q_p = N_s e$ and $M_p = N_s m_e$.

Organize the equation to solve$(a_{np}$for$)'$ =the$a$dimensionless$_{np\ E(xH_{np})meD_e T2} =$ (EEfield(x_{pn}))expression:'

$$(E(x^n{}_p))' = \underline{D}_H \underline{T} m^2 \underline{e}_e E(x^n{}_p)$$

Charge Density

Wechargesnow calculateto the gridthe chargepoints densityaccordingin thetosimulation.the distribution$W$ is the function that weighsabove.theIn

actual unitsx_{np} we have x_g scheme discussed

$$\rho_{ng} = \frac{Q}{V_{cell}} \Sigma W(x_{np}, x_g)$$

The function W provides the fractional weighting to the grid points.

Consider a particle at position $x^n{}_p$ with $g + 1 > x^n{}_p > g$, where g is a grid point. Suppose

$x_{np} = g + fraction$. Then

$$x_g \mathrel{+}= x^n{}_p \cdot (1 - fraction)$$

$$x_{g+1} \mathrel{+}= x^n{}_p \cdot fraction$$

Therefore, the weight of the charge at position x_g and x_{g+1} from particle $x_p{}^n$ is:

$$W(x^n{}_p, x_g) = x^n{}_p \cdot (1 - fraction)$$

We need to relate the actual plasma$W(x_{np}$,density$x_{g+1})$ =n ($x$electrons/volume$_{np}$ ·

$fraction$) to the dimensionless charge density. Suppose there are N_c superparticles

per V_{cell}. Therefore, $N_c = N_p/Ng$

Wewherecan$N$express$_p$ is the thetotalparticlenumbernumberof superparticles,density n_p as:and Ng is the total number of grid points.

$$n_p = N\overline{V_{scell}N_c}$$

Where N_sN_c is the total number of particles and V_{cell} is the volume of a cell. We can solve

this for V_{cell} giving

$$V_{cell} = \overline{N_snN_c}$$

Substituting into the expression n = $\overline{V^{Q_{cell}}}$ gives

Rewriting the dimensionless chargeVQ_{cell}=density:$VN_{cellse} = N_se$ $N_snN_c = \underline{ne}N_c$

$$(\rho_{ng})' = \rho_{ng}\ 2\underline{D}m\underline{T}_{e2}\epsilon\underline{e}_0 = VQ_{cell}\Sigma W(x_{np}, x_g)\ 2\underline{D}m\underline{T}_{e2}\epsilon\underline{e}_0$$

$$(\rho_{ng})' = \frac{n_e N_c 2 D_m T_{e2} \epsilon_0}{e} \Sigma W(x_{np}, x_g)$$

We can rewrite this expression(using$\rho_{ng})'$ =the$2\underline{n}$electron$\frac{m_{e2_e} D \epsilon_0 T N_{2c}}{e} \Sigma W$plasma($x_{np}$, $x_g$frequency:)

$$\omega_{2p} = \frac{m n_e e \epsilon^2_0}{e}$$

Recalling that $N_c = N_p/Ng$, we have for the final expression for the dimensionless

charge density

$$(\rho_{ng})' = \frac{D\overline{T^2_2 N g \omega_{2p} N_p}}{e} \Sigma W(x_{np}, x_g)$$

Chapter IV. Program Tests

In this chapter we will perform some simple tests to verify the potential, electric field, and mover parts of the algorithm. We will consider cases where an analytic solution exists and compare the results with the PIC simulation.

A. Potential and Electric Field Calculation Tests

1. Charge Density = 0

In the absence of charge density, the Poisson's equation is

$$\frac{d^2\phi}{dx^2} = 0$$

The solution is a linear potential function. And the electric field is a constant equal to the negative of the potential slope. We set $V_0 = constant\ 1$ and $V_{Ng+1} = constant\ 2$ and the resulting linear potential and constant electric field are shown in figure 4~5.

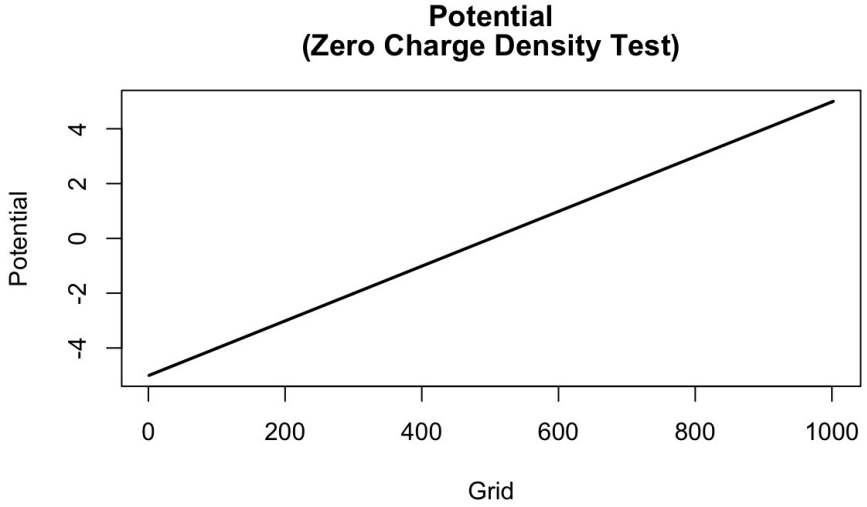

Figure 4.1: Dimensionless potential profile for the zero charge density test.

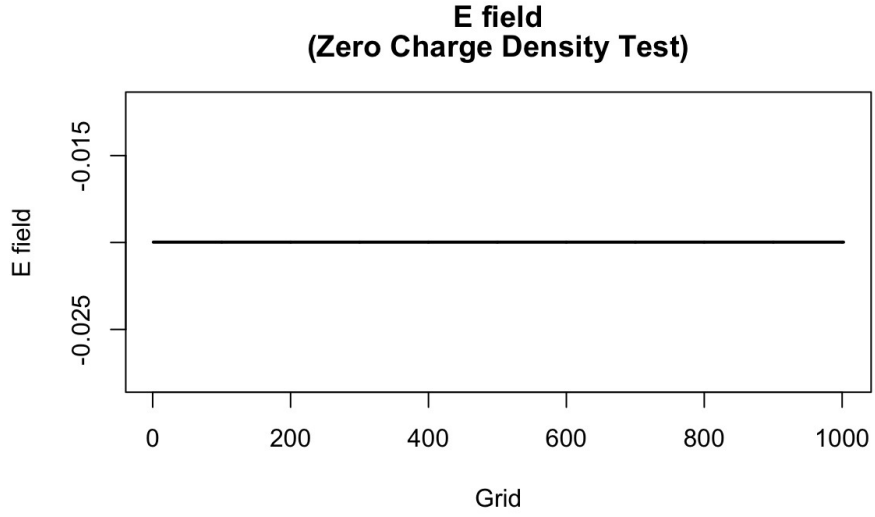

Figure 4.2: Dimensionless E field profile for the zero charge density test.

2. Constant Charge Density

We now set the charge density ρ to a non-zero constant at every grid point and set both boundary potentials to be zero. We expect a parabolic shape of the potential as a solution to $\frac{d}{d^2x}\frac{\phi}{} = -\epsilon\frac{\rho}{} =$ non-zero constant

$$2 \qquad 0$$

as shown in Figure 4.3 . The corresponding electric field is then a linear function with a positive slope passing through x = 0 at the midpoint as shown in Figure 4.4 .

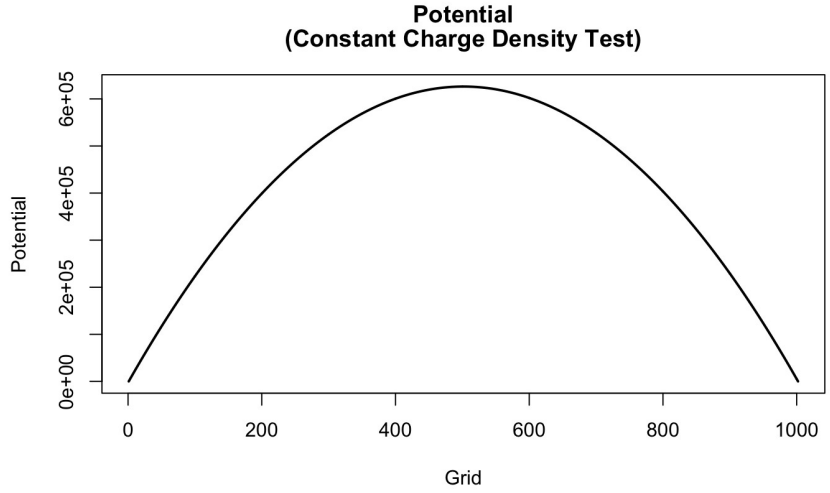

Figure 4.3: Dimensionless potential profile for the constant charge density test.

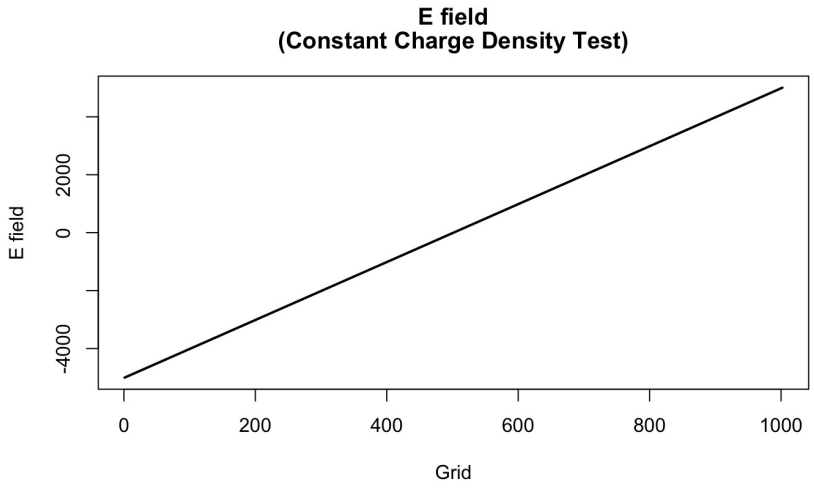

Figure 4.4: Dimensionless E field profile for the constant charge density test.

3. Single Particle Charge Density

In this test we place one stationary positively charged particle at the middle of the region with the potential at the endpoints set equal to zero. The charge density will be zero everywhere except at the position of the particle where the potential has a maximum. The

electric field is then constant in the regions where there is no charge, negative in the left half of the regions, positive in the right half and zero at the particle position.

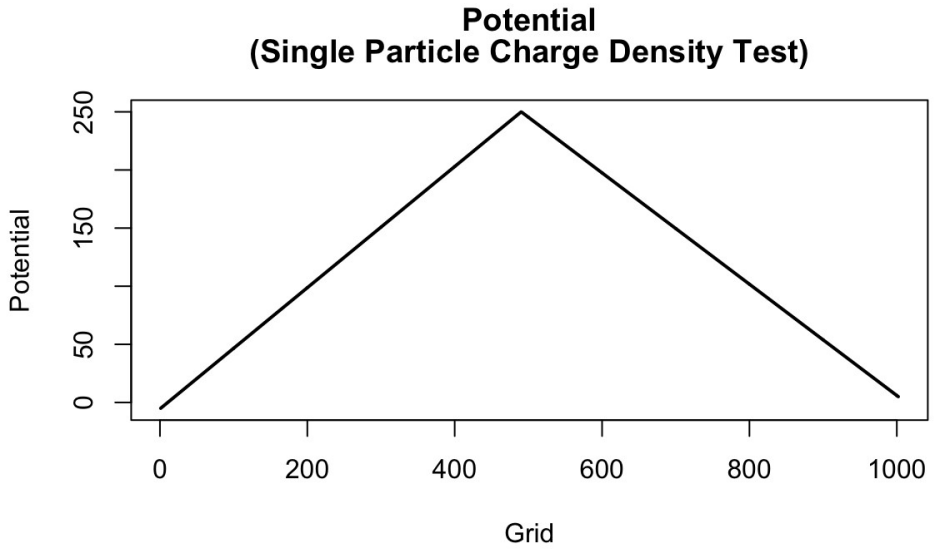

Figure 4.5: Dimensionless potential profile for the single particle charge density test.

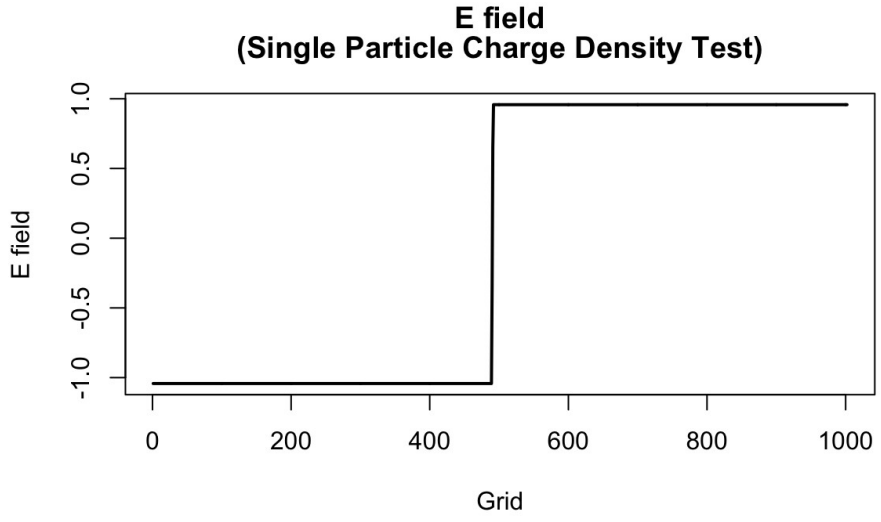

Figure 4.6: Dimensionless E field profile for the single particle charge density test.

4. Two Particle Charge Density

Here we place two particles in the system, both stationary and placed symmetrically.

Figure 4.7 shows that our analytic result is the same as the simulation one.

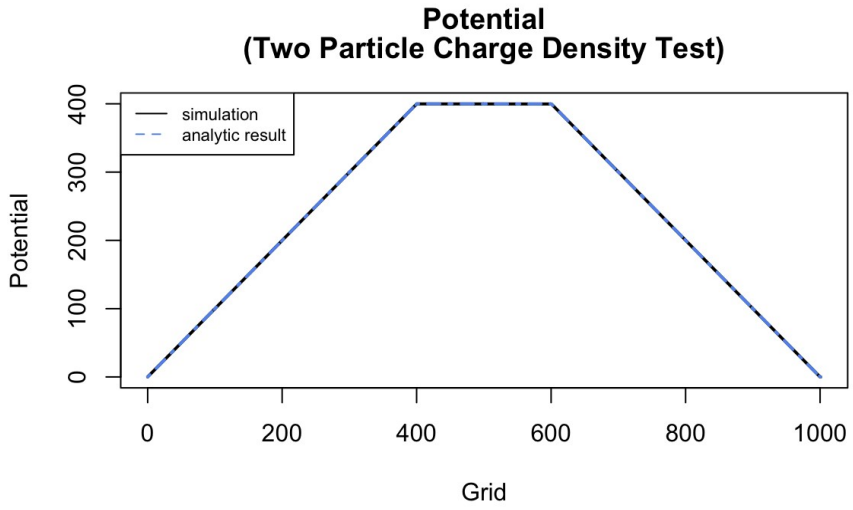

Figure 4.7: Dimensionless potential profile for the two particle charge density test.

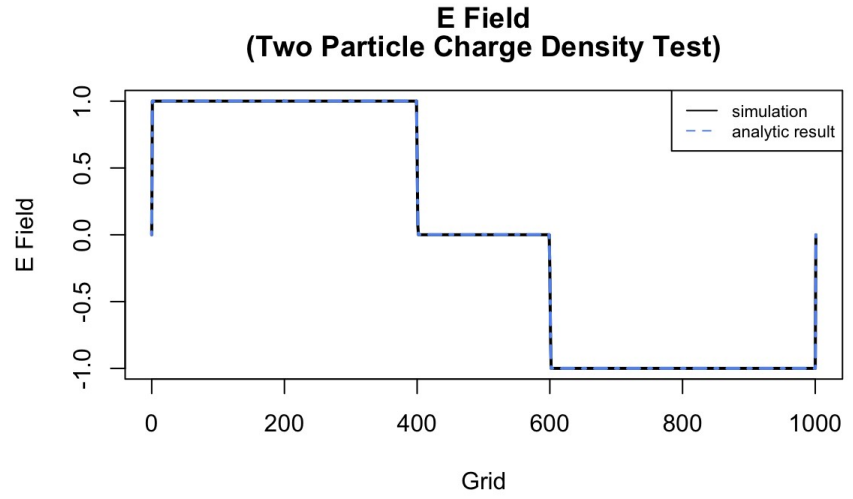

Figure 4.8: Dimensionless E field profile for the two particle charge density test.

B. Mover Tests

1. Linear Potential

Here we test the mover function for a given potential. We first define a linear potential distribution, so that the E field, as well as for the acceleration of the particle, will be constant. Under constant acceleration, the displacement should be

$x = x_0 + v_0 t + {}^1\!/_2\, \overline{a} t^2$. Figure 13 shows that our simulation result agrees with the analytic result precisely.

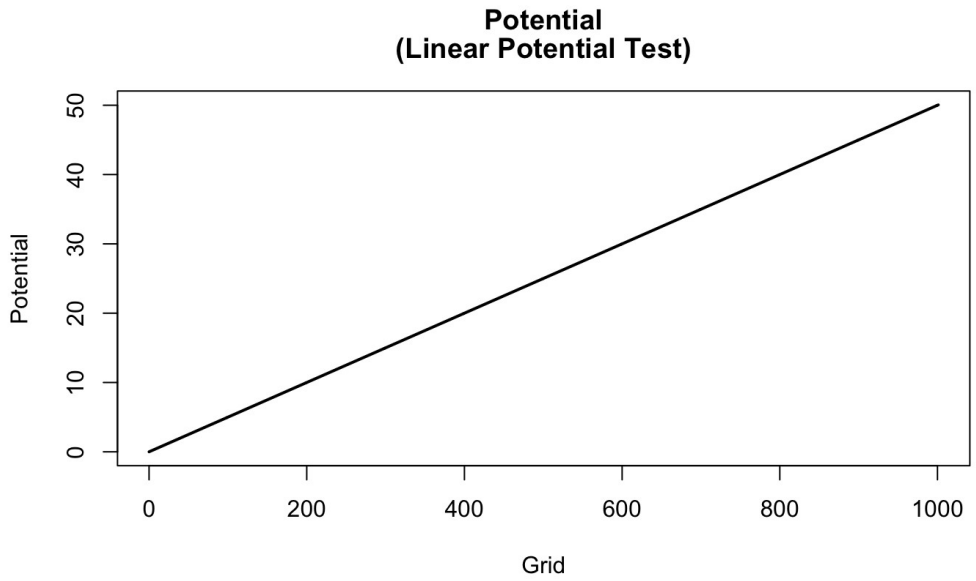

Figure 4.9. Dimensionless potential profile for the linear potential test.

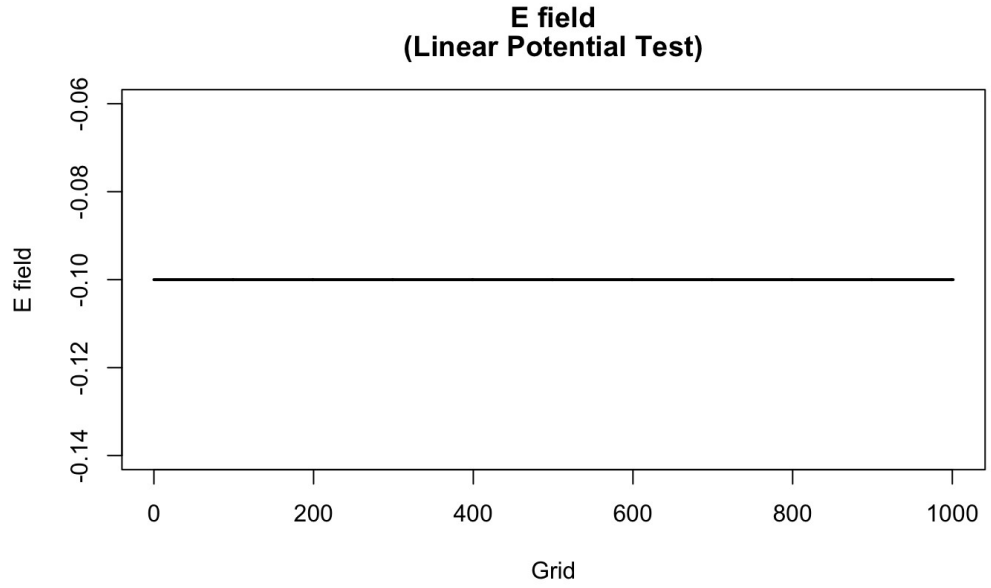

Figure 4.10. Dimensionless E field profile for the linear potential test.

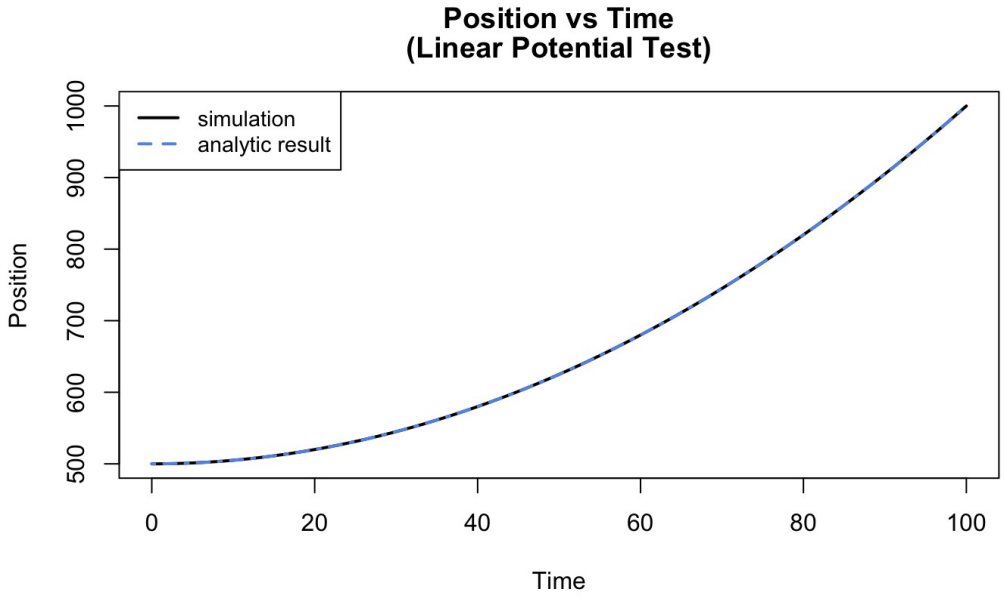

Figure 4.11. Dimensionless Position vs Time plot for both simulation and analytic results.

2. Harmonic Oscillation

In this test a negatively charged particle is in the middle of the potential described by

Figure 4.3. For a negative charge this potential represents a harmonic well and we expect

the particle to undergo simple harmonic motion over time. Figure 4. 12 confirms this prediction

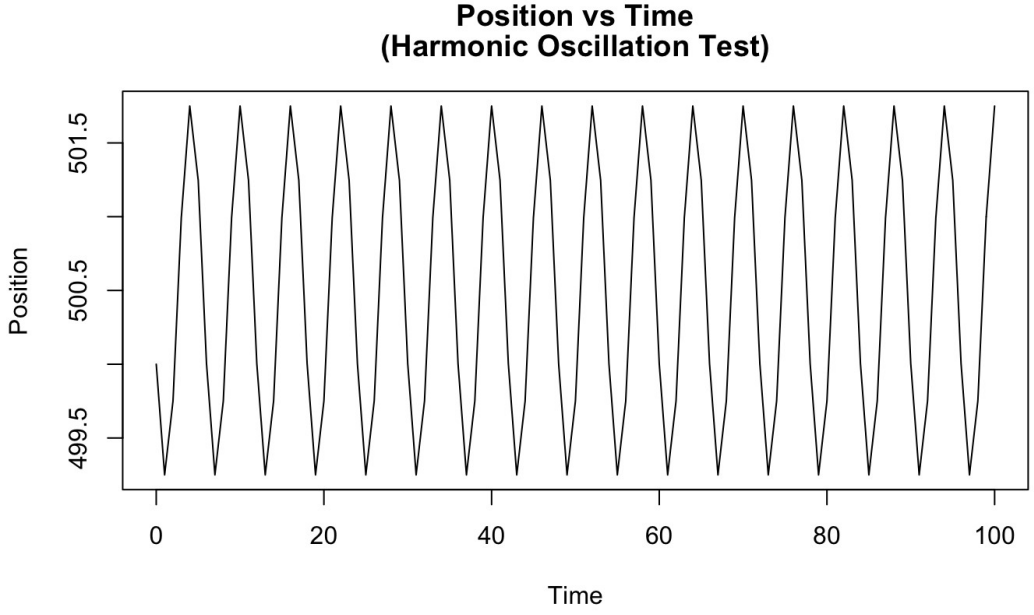

Figure 4.12. Dimensionless Time vs Position plot for the harmonic oscillation test.

Chapter IV. Results

Simulation Conditions

In this chapter we discuss simulations that are approximately equivalent to static afterglow experiments (see Chapter I). Electrons and ion superparticles are uniformly but randomly distributed throughout a gap, with the boundary potentials set at 0 V in equal numbers. The electrons and ion velocities are initialized according to Maxwell-Boltzmann distributions characterized by an electron temperature T_e and an ion temperature T_i. This results in an initial potential profile that has $\phi = 0$ throughout the gap. However, due to the ambipolar diffusion effects discussed in Chapter 1, electrons near the boundaries are quickly lost to the wall and sheath regions with an excess of

positive charge are formed. This results in electric fields forming near the boundaries and the potential of the quasi-neutral middle region to increase relative to the boundaries. Based on the discussion of Debye length in Chapter I, we expect the spatial extent of the sheath regions to scale with the Debye length.

We initially ran two sets of parameters (Table 1), each with seven different numbers of time steps Nt: 5000, 2500, 1000, 500, 200, 100, 50, and 20.

Table 5.1. Groups of parameters used for the simulation.

	Electron Temperature (K) T_e	Plasma Density n_p (m^{-3})
Group 1	30000	10_{15}
Group 2	30000	$_{17}$

10

A. $T_e = 30000$ K, $n_p = 10^{15}$ m^{-3}

Figure 5.1 shows the potential profile evolution for the Group 1 parameters, considered our default conditions for these simulations. We observe a well-defined sheath for each simulation time, though the sheath width depends on the simulation time N_t. We also observe an increase in the quasi-neutral plasma potential when N_t increases from 500 to 2500. However, for $N_t > 2500$ this potential begins to decrease and at $N_t = 10000$ it is

close to that of N, = 500. Since electrons and ions are not replenished after absorption by the boundary, we expect the plasma potential to continue to decay until all particles leave the system. However, for these simulation conditions it would take an impractical amount of computer time (days) for all particles to leave.

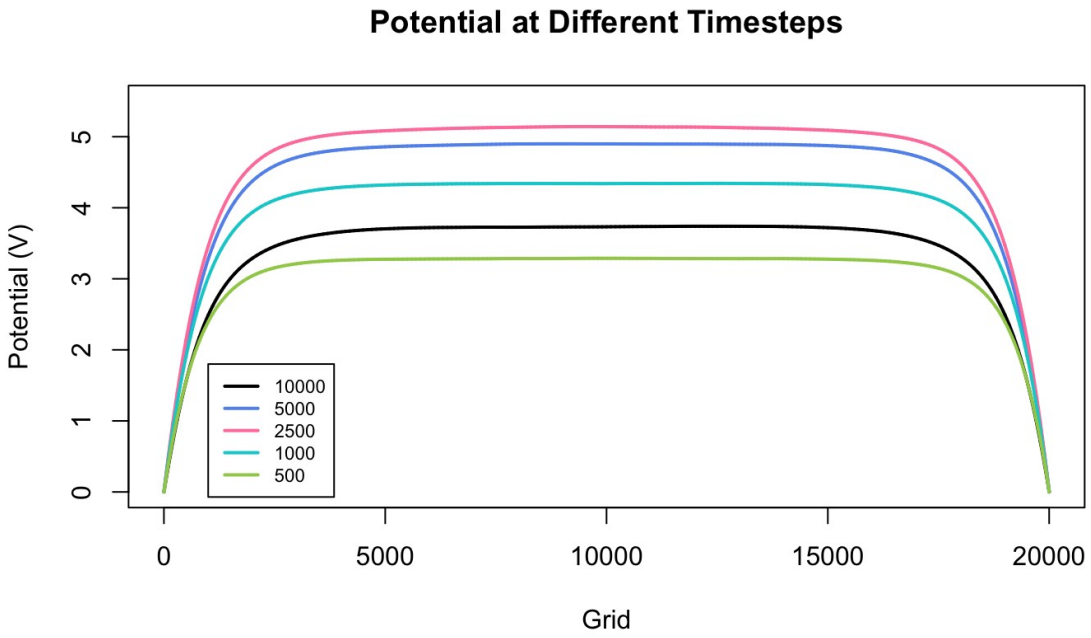

Figure 5.1. Potential profile for different numbers of total time-steps N_t = 500, 1000, 2500, 5000, and 10000.

To better understand the evolution of the system under these conditions, we plot the particle loss rate for electrons and ions in Figure 5.2. We find that electrons initially have a rapid loss rate, which quickly drops. The ion loss rate initially increases and then appears to flatten out. At $N_t = 2500$, the electron loss rate intersects with the ion loss

rate. After this intersection, the electron loss rate continues to decrease while the ion loss rate stays almost constant, but is actually decreasing slowly (not apparent in Figure 5.2). We can account for these results as follows. Initially when the electron flux towards the wall is high in the system, an excess of positive charge rapidly builds up in the sheath regions, increasing the plasma potential. However, when $N_t > 2500$. the loss rate of electrons becomes less than the loss rate of the ions. Since the ions are now being lost at a higher rate than the electrons, the plasma potential begins to decline.

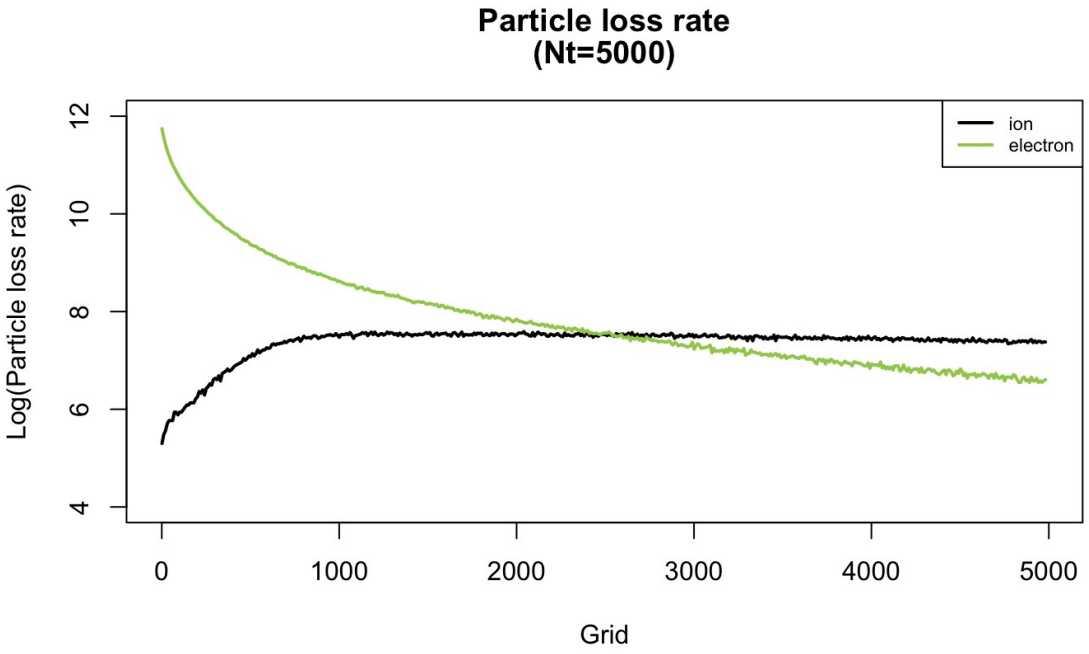

Figure 5.2. Particle loss rate for electrons and ions respectively for $N_t \, up \, to \, 5000$.

These considerations are supported by the evolution of the charge density. Figure 5.3 shows the charge density in the system at three different phases in the plasma evolution:

1) $N_e\ loss\ rate > N_i\ loss\ rate$, 2) $N_e\ loss\ rate = N_i\ loss\ rate$, 3) $N_e\ loss\ rate < N_i\ loss\ rate$.

We observe that at $N_t = 500$, there is relatively more positive charge in the sheath

while

sheath.region, This resultafter alsoconforms, thetopositiveour

previouschargeanalysis:densityduringstarts tothedecreasephases whereinthe the electron

loss rate exceeds that of the ion, the ions are more attracted to the wall potential, resulting in the accumulation of positive charge within the sheath region. As the electron loss rate continues to drop and the ion loss rate starts to catch up and eventually surpasses that of the electron, ions are more prone to stay in the system.

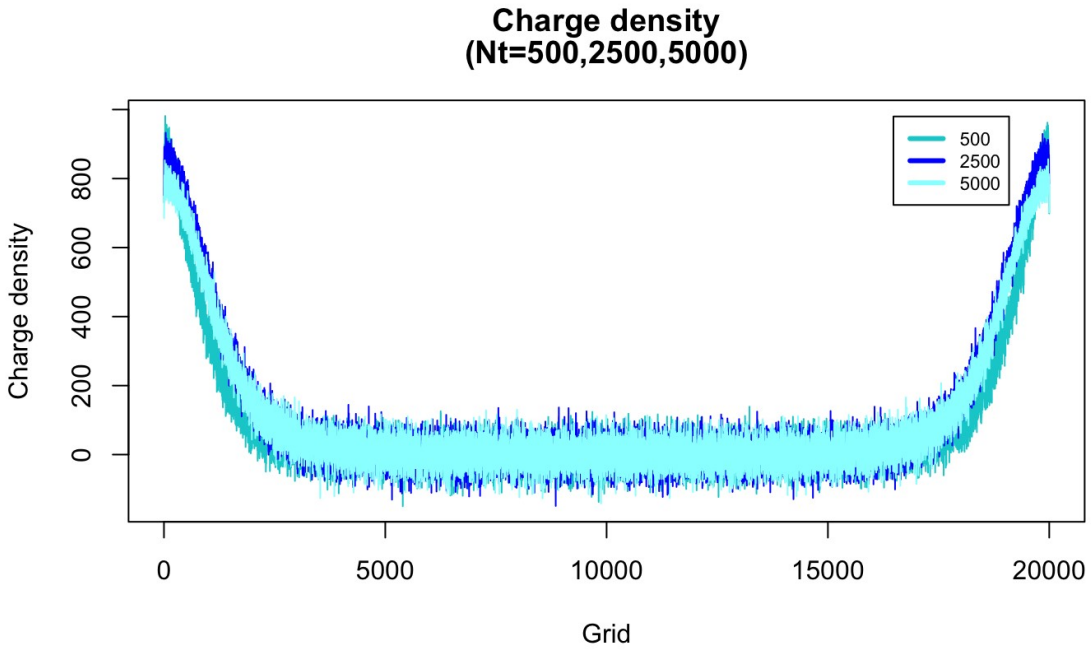

Figure 5.3. Charge density for $N_t = 500$, 2500, and 5000.

In addition to the evolution of the potential and charge density, the velocity distributions of the electrons and ions also evolve in time. In Figure 5.4 we have plotted the electron and ion velocity distributions at $N_t = 50$ and $N_t = 10000$ time steps, compared to the original Maxwell-Boltzmann distributions. At $N_t = 50$ the distributions are very similar to the initial distributions, but by $N_t = 10000$ there has been considerable evolution of the distributions, especially in the case of electrons. The dramatic change in the electron distribution is to be expected, since due to the steep potential energy barrier due to the sheath formation, high energy electrons will be preferentially lost, shifting the distribution to lower energies.

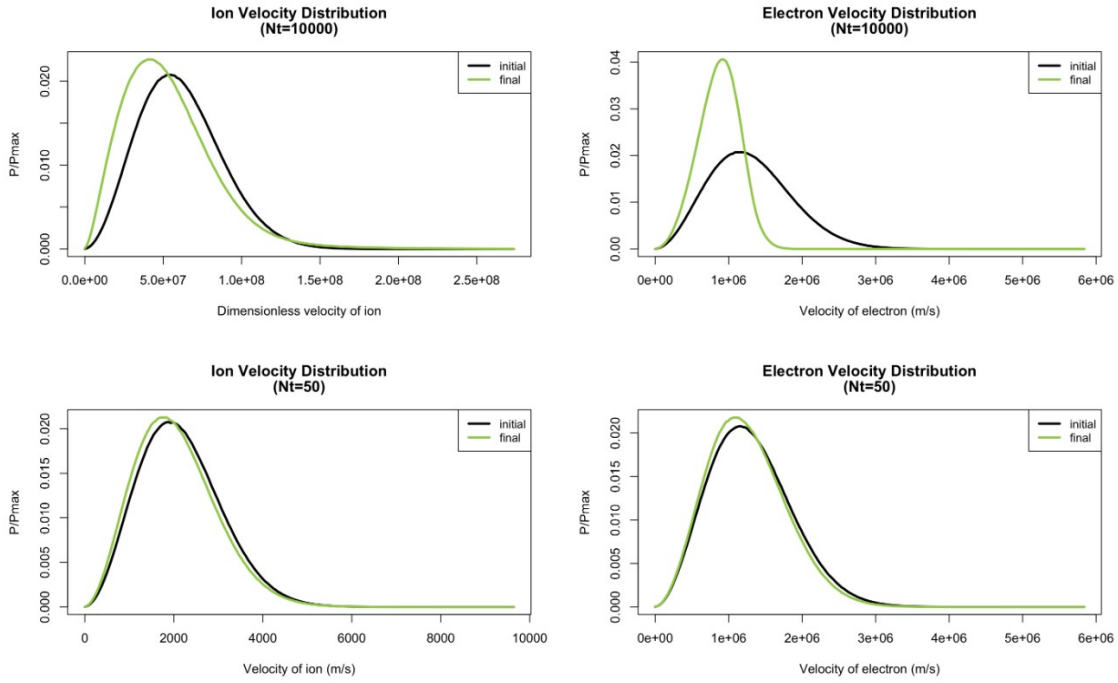

Figure 5.4. Initial and final velocity distribution for electrons and ion respectively, as well as for $N_t = 10000$ and $N_t = 50$ respectively.

The simple ambipolar diffusion theory predicts that the electron and ion loss rates should equalize in the fully developed afterglow. Although we do see the predicted decrease in electron wall flux and increase in the ion wall flux, as shown in Figure 5.2 the system does not reach the ideal steady-state where the electron flux equals the ion flux in the steady state. However, given the results in Figure 5.4, as well as the fact that the electron and ion numbers decrease over time, we do not expect an ambipolar steady state can be achieved. The simple ambipolar theory assumes fixed values of the electron and ion concentrations and temperatures, which is clearly not the case under these conditions. In fact, without some means of replenishing the electrons and ions to maintain the

concentrations and velocity distributions, the system can never truly achieve a steady state. This is especially true for electron behavior.

B. $T_e = 30000$ K, $n_p = 10^{17}$ m^{-3}

The inability to achieve an ambipolar steady-state under our standard conditions due to the continuing rapid loss of particles and evolution of the velocity distributions (especially the electrons) suggests that higher plasma densities might give a result closer to the ideal ambipolar theory. At higher plasma densities the sheath should contract since according to Equation 1.1 the Debye length should decrease, causing the sheath to contract and increasing the plasma potential, and thereby limiting the loss of electrons.

In Figure 5.5 we show the evolution of the plasma at the initial conditions of $T_e = 30000$ K, $n_p = 10^{17}$ m^{-3}. As expected, we observe a contraction of the sheaths compared to the standard conditions of $T_e = 30000$ K, $n_p = 10^{15}$ m^{-3}. (Figure 5.1) . In Figure 5.6 we show the loss rates of the electrons and ions, and Figure 5.7 gives the evolution of the velocity distributions at 5000 timesteps.

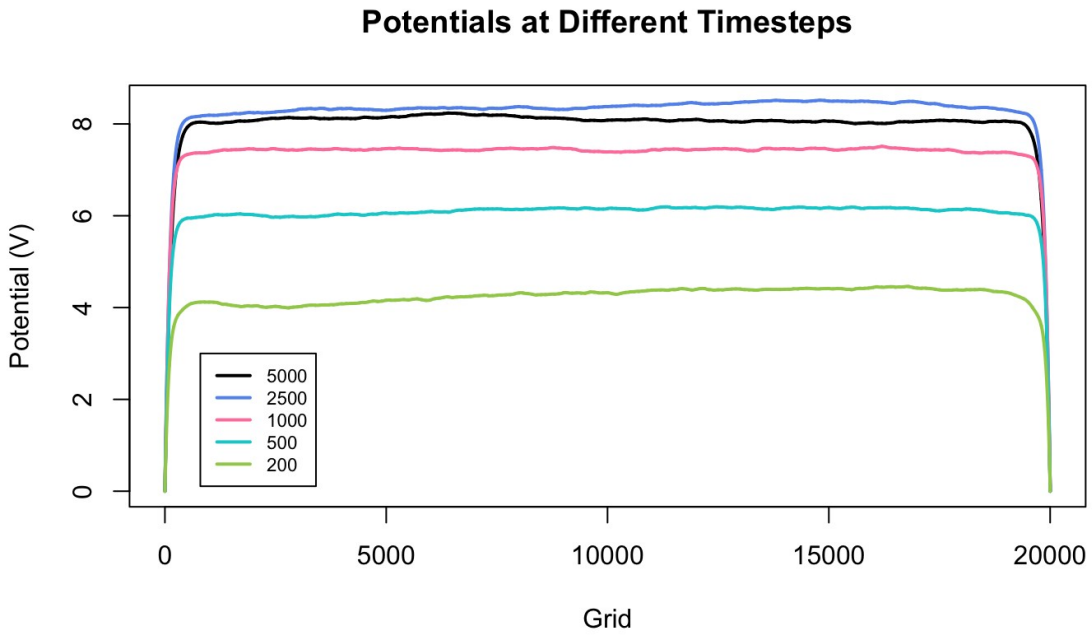

Figure 5.5. Potential profile for different numbers of total time-steps $N_t = 200$, 500, 1000, 2500, and 5000.

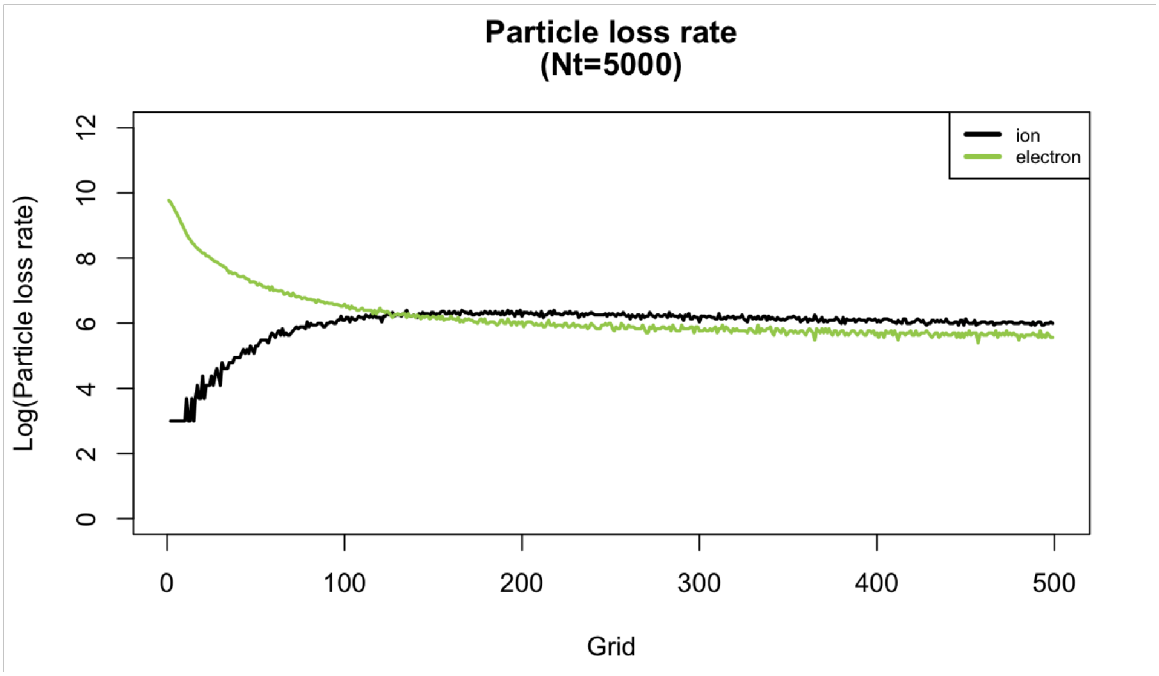

Figure 5.6. Particle loss rate for electrons and ions respectively for $N_t = 5000$.

From the particle loss rate evolution (Figure 5.6) we see a different pattern compared to the previous Group 1 parameter results. With $n_p = 10^{17}$, the electrons and ions both converge to stable values. The loss rates of both species are also very close to each other. Although not exactly the same as expected in the ideal case, this result is closer to representing an ideal ambipolar diffusion scenario. The evolution of the velocity distributions over time from Figure 5.7 confirms that the electron velocity distribution still maintains a quite stable shape at least up to $N_t = 5000$. These results are consistent with the better confinement of the quasi-neutral plasma due to the higher plasma density.

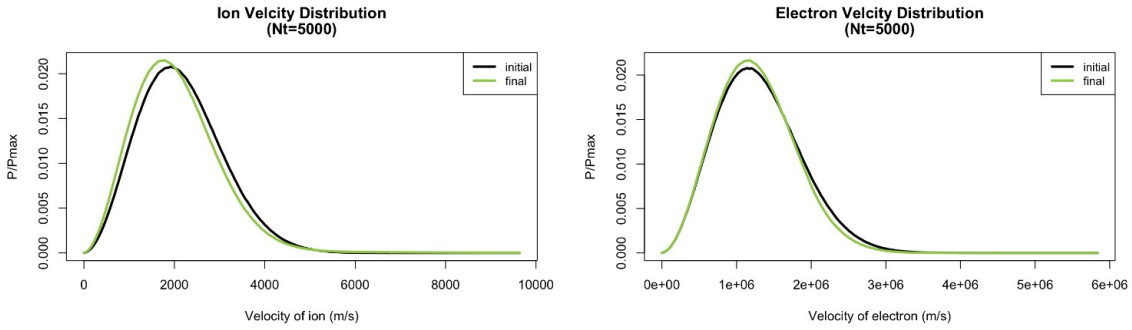

Figure 5.7. Initial and final velocity distribution for electrons and ions respectively, $N_t = 5000$.

C. Sheath Width Dependence on T_e and n_p

Finally it is of interest to vary n_p and T_e to verify the assumptions that the sheath width should scale with the Debye length. Recall that the expression for the Debye length is given by

$$\lambda_D = \left(\overline{\epsilon_0 n K_e T_{2e}} \right)_{1/2} \qquad (1.1)$$

As discussed in the Introduction, the Debye length is the characteristic length over which the plasma can deviate from neutrality. Thus, we expect the sheath widths at the boundaries to be strongly correlated with the Debye length. There is no universally accepted precise definition of the sheath width, but if we define the sheath width as the distance to 90% of the maximum potential, we can compare the Debye length to the sheath width for different values of n_p and T_e.

As is evident from the results presented above, another issue in making such comparisons is that the system is not static and continues to evolve over time. Nevertheless, it is possible to make semi-quantitative comparisons if we confine the condition to early enough in the evolution so that the electron energy distribution has not significantly evolved and a significant decrease in electron superparticle numbers has not occurred, but evolved enough where the potential profile in the central region of the region is relatively stable. In the cases discussed below the average electron energy was within 1% of the starting average energy, and the electron superparticle numbers had decayed to less than 4% from the starting values.

In Figure 5.8 we show the potential profile near the boundary for plasma densities of 1e14, 1e15, and 1e16 after 500 time steps, all at $T_e = 30000\ K$ and $T_i = 30000\ K$. The

potentials have been normalized by their maximum values near the middle of the region so that the sheath profiles can be compared on the same scale. In Figure 5.9, we show the comparison between the Debye length and the sheath widths. The ratio of the sheath width to the Debye length is of order 1 for all cases as expected. The ratio of sheath width to Debye length ranges from about 1 for $n_p = 10^{14}$ to about 3 for $n_p = 10^{16}$. Despite

this variation, the strong correlation of sheath width with Debye length is evident. Given the arbitrariness of our sheath width definition and the absence of any precise relation between the sheath width and Debye length, we consider this level of agreement to be satisfactory.

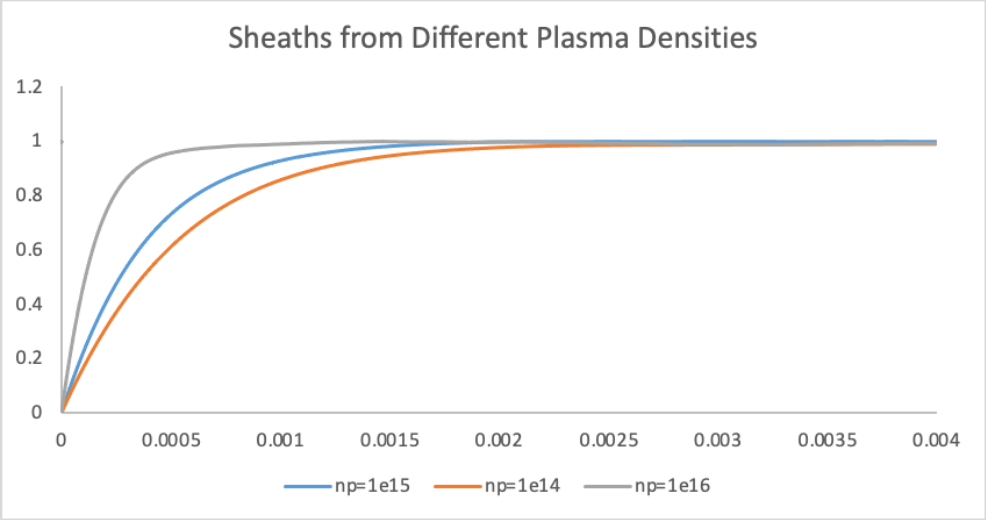

Figure 5.8. Potential in sheath regions for $n_p = 10^{14}$, 10^{15}, and $10^{16}\ m^{-3}$. The potentials have been normalized by their maximum values.

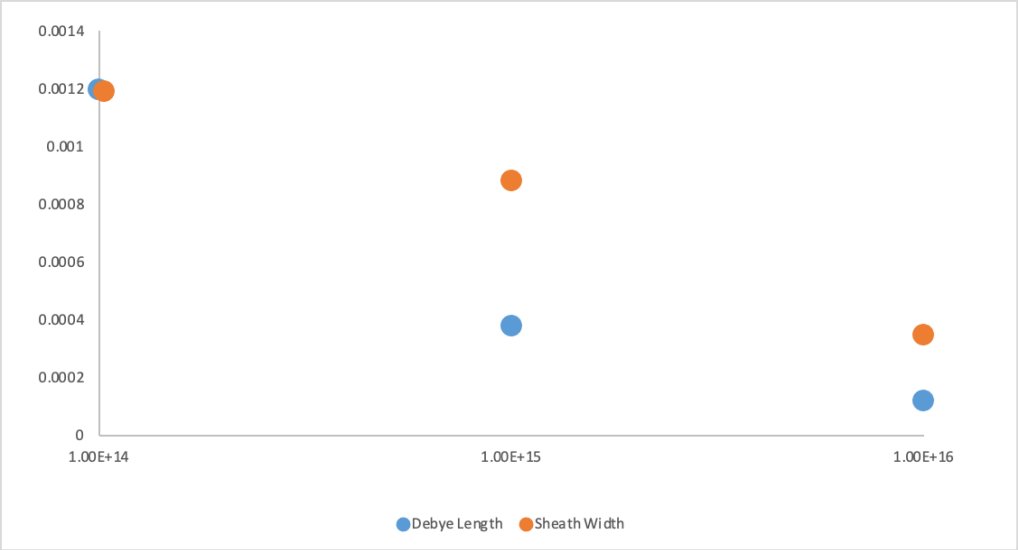

Figure 5.9. Debye length and sheath width comparison.

In Figure 5.10 we show the effect of varying the electron temperature. A good correlation exists between the sheath width and the Debye length, as observed in Figure 5.11. In this case the ratio varies between 2.7 and 2.1 for T_e varying between 10000 K and 30000 K,

again illustrating the strong correlation between the Debye length and the sheath width.

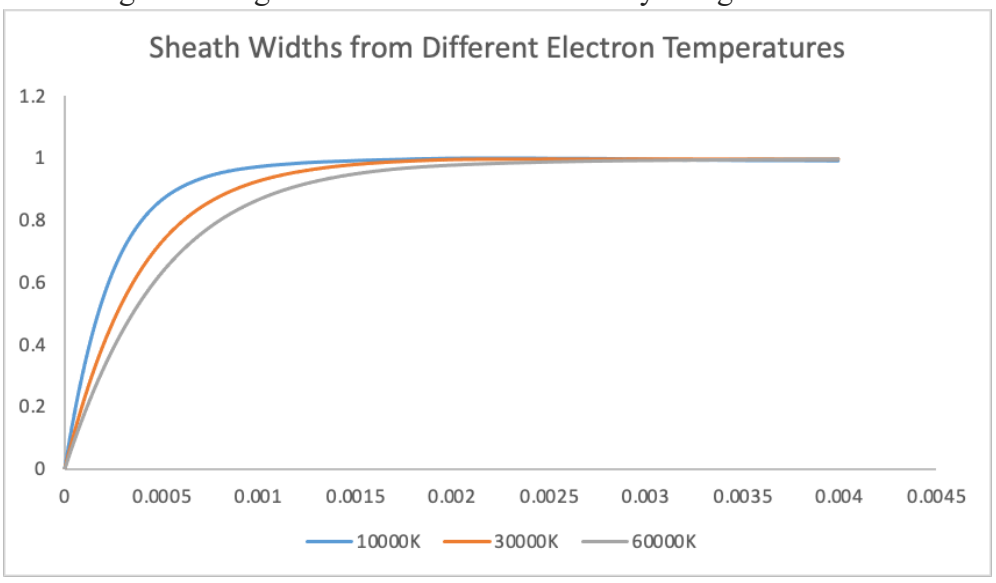

Figure 5.10. Potential in sheath regions for $T_e = 10000\ K, 30000\ K,$ and $60000\ K$. The potentials have been normalized by their maximum values.

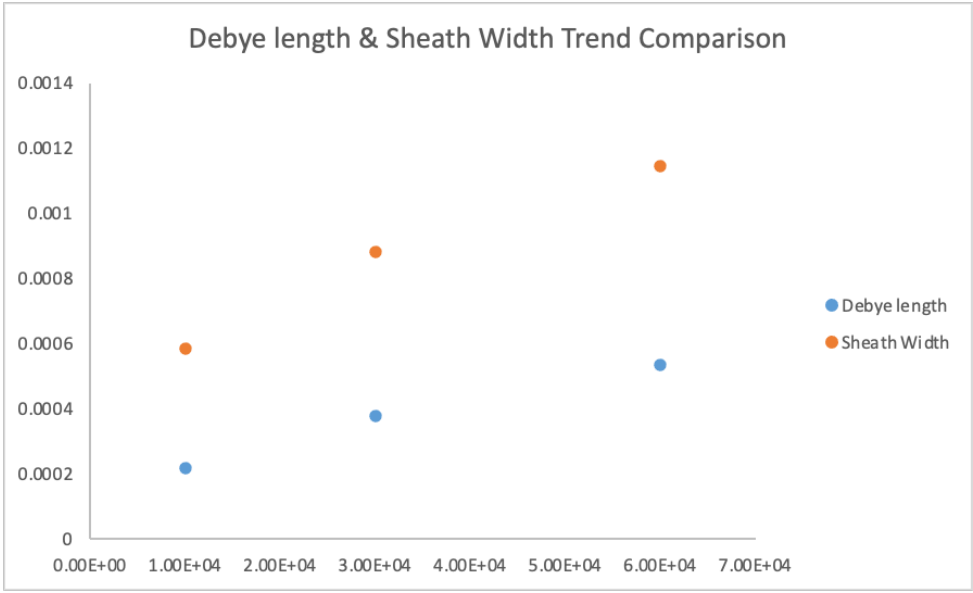

Figure 5.11. Debye length and sheath width comparison as a function of T_e.

We conclude that the observed sheath widths are qualitatively consistent with basic plasma theory with the expected scaling with the Debye length.

VI. Conclusions and Future Work

We have developed a Particle-in-Cell (PIC) model with collisions for a one-dimensional electrostatic plasma. We have confirmed our program is consistent with basic plasma behavior, particularly with regard to plasma evolution by ambipolar diffusion and sheath formation. The relevance of the theoretical Debye length is confirmed and the results are in qualitative agreement with the expected relation between the Debye length and and the sheath formation with respect to variations of plasma density and electron temperature.

Although we did not achieve conditions that reflect the ideal ambipolar diffusion case, the results indicate that better agreement occurs with higher plasma densities, as expected. The program provides a firm foundation for further studies of the plasma dynamics of weakly-ionized plasmas that are commonly used in technological applications.

There are many opportunities for further study and refinement of the simulation. A wider range of conditions of plasma density and electron temperature should be explored. We did not examine the effect of changing gas pressure which would affect the collision dynamics. In addition, more realistic electron-atom and ion-atom scattering models could easily be introduced. We would also like to explore mechanisms that would help maintain fixed electron and ion temperatures and densities while allowing the formation of sheaths. For example, an electron and ion generation term can be introduced, that would perhaps correspond to UV photon ionization processes (work on a preliminary version of this approach is already underway). Secondary electron emission from the electrode could also be easily introduced.

Due to the one-dimensional nature of our program, the simulation can only consider electrostatic forces. A further extension could consist in developing the program into two-dimensional simulation where more realistic experimental geometries and magnetic forces could be introduced. With the basic structure presented here in place, all of these refinements could be implemented in a straightforward manner. With some of the above refinements a robust comparison to experimental results, as well as detailed plasma theories, could be achieved.

VII. Bibliography

[1] Park, Sanghoo, et al. “Electron Characterization in Weakly Ionized Collisional Plasmas: From Principles to Techniques.” *Advances in Physics: X*, vol. 4, no. 1, 2018, p.

1526114., doi:10.1080/23746149.2018.1526114.

[2] “Basic Concepts.” *Fundamentals of Plasma Physics*, by Paul M. Bellan, Cambridge University Press, Cambridge, 2006, pp. 1–33.

[3] Manfredi, Giovanni, and Fabrice Valsaque. ‘Plasma-Wall Transition and Sheath Formation’. *Vide*, vol. 306, 01 2003, pp. 810–835.

[4] Liberman, Michael, and Michael Lichtenberg *Principles of Plasma Discharges and Materials Processing*, John Wiley & Sons, Inc, 1994, pp. 16-19.

[5] Liberman, Michael, and Michael Lichtenberg *Principles of Plasma Discharges and Materials Processing*, John Wiley & Sons, Inc, 1994, p. 452.

[6] Van Sark, Wilfried G. J. H. M. ‘Methods of Deposition of Hydrogenated Amorphous Silicon for Device Applications’. *Advances in Plasma-Grown Hydrogenated Films*, edited by Maurice H. Francombe, vol. 30, Academic Press, 2002, pp. 1–215, https://doi.org10.1016/S1079-4050(02)80004-7. Thin Films and Nanostructures.

[7] E. Havlíčková, E. ‘Fluid Model of Plasma and Computational Methods for Solution’. WDS’06 Proceedings of Contributed Papers, Part III, 2006, pp.180-186.

[8] Zhang, W., et al. 'Analysis of non-equilibrium phenomena in inductively coupled plasma generators'. *Physics of Plasmas*, vol. 23, no. 7, 07 2016, https://doi.org10.1063/1.4958326.

[9] Thornton, Stephen T. , and Jerry B. Marion *Classical Dynamics of Particles and Systems*, Cengage Learning, 2003.

[10] Ghojogh, Benyamin, et al. 'Sampling Algorithms, from Survey Sampling to Monte Carlo Methods: Tutorial and Literature Review'. *ArXiv [Stat.ME]*, 2020, http://arxiv.org/abs/2011.00901. arXiv.